ESTIMATING $\vec{\omega}(\vec{k})$ IN AN UNSTEADY, WIND-GENERATED SURFACE WAVE FIELD FROM THE *2D* COMPLEX WAVELET TRANSFORM OF THE SURFACE SLOPE

G. R. Spedding
Department of Aerospace Engineering, University of Southern California, Los Angeles, California, U.S.A.

J. Klinke
Scripps Institution of Oceanography, University of California, San Diego, California, U.S.A.

and

S. R. Long
NASA GSFC/WFF, Wallops Island, Virginia, U.S.A.

Abstract. The initial formation and growth of capillary-gravity waves under wind-induced surface stress is studied by measurement of the instantaneous, *2D* distribution of the along-wind slope at a fixed fetch. A new technique, using information from the complex *2D* wavelet transform, is described for the calculation of the local, instantaneous dispersion relation. The technique is validated on simple test fields. The dispersion relation measured from the wave tank data is consistent with predictions from linear stability theory at early times, but departures can be noted later on. Some physical interpretations are offered, and possible nonlinear mechanisms are discussed.

1 Introduction

Classical linear stability analysis has been partially successful in predicting the generation and growth of the initial wave field on a calm water surface following an impulsive start in the wind stress. However, neither the Phillips resonant interaction (Phillips, 1957; Phillips, 1977), nor the Miles critical layer instability mechanism (Miles, 1957; Miles, 1959) has been able to incontrovertibly account for laboratory and field measurements of growth rates and wave initialisation. Kawai (1979) made careful measurements of the initial growth of wind generated surface waves, and combined this with a stability analysis by numerical integration of the Orr-Sommerfeld equation with initial and boundary values suggested by the experimental data. It was found that linear, shear flow instability mechanisms could successfully predict growth rates, phase speeds, and wavenumber-frequency relations in the observed wave field, to within experimental accuracy. It was further pointed out that the subsequent evolution of long-crested to short-crested waves could not be expected to be governed by linear mechanisms, as indeed was indicated by 'complicated movements of spectral peaks'. These spectra were quasi-steady estimates, computed by the maximum entropy method (*cf* Press *et al.*, 1992) on data segmented in time.

Following recent advances in local space-scale decompositions by means of wavelet functions, it is now possible to perform a systematic quantitative analysis of such unsteady phenomena, without some of the limitations imposed by the Fourier decomposition, and where the balance between resolution in physical and spectral space, scales automatically with wavenumber, within the limits
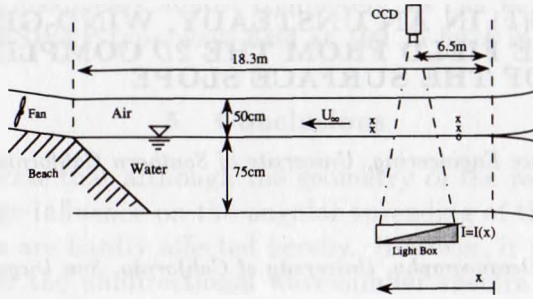
Fig. 1.   Simplified schematic of the wind-wave generation facility. The x's mark approximate locations of Pitot tubes, and a capacitance wire probe for wave elevation is marked by an 'o'. The fan control, 1D digitising of Pitot tube and wave height data, and sampling of the *2D* video signal are synchronised using 3 personal computers and one Sun workstation.

prescribed by the uncertainty principle. The objective of this paper is to describe the development of a method for the measurement of spatially-localised frequency and wavenumber relations of unsteady wind-generated surface waves, and to give examples of its initial application to recent, *2D*, instantaneous wave slope data. This will include the later times when nonlinear mechanisms may be anticipated to be significant.

2   Experimental data

The experiments were conducted at the NASA Wallops wind-wave interaction facility, which is described in detail in Long (1992). The aspects of significance to this paper are shown in Fig. 1. Air is drawn by suction over a 75 cm deep water channel over a working section of approximately 18m length and 0.9m width. The air gap over the still water surface is 46 cm. Observations of the streamwise surface slope were made at a fetch of 6.5m, using an Imaging Slope Gauge (ISG) with a field of view of approximately 18.5 x 14cm. The single experimental run treated here was made with a mean reference velocity, $U_5 = 5.2$ m/s (measured 5cm above the surface, and 15 cm upstream of the ISG). Digitizing of the video-encoded CCD signal began 7s after the fan was turned on, at which time $U_5 = 5.0$ m/s. By frame #50, 8.6s after fan-on, the steady value of U_5 had been reached. The x, y and z axes of a Cartesian coordinate system run streamwise, spanwise, and vertically up from the water surface, respectively.

The physical problem is thus somewhat complicated – not only does it involve temporal and spatial growth of viscous boundary layers in both water and air, but the initial conditions and start up are much less homogeneous in space and instantaneous in time, than one would perhaps prefer, and careful physical interpretations must be made in this light.

The ISG works on principles described in Jähne and Reimer (1990). A strong, homogeneous (in y) light source illuminates a rectangular box filled with par-
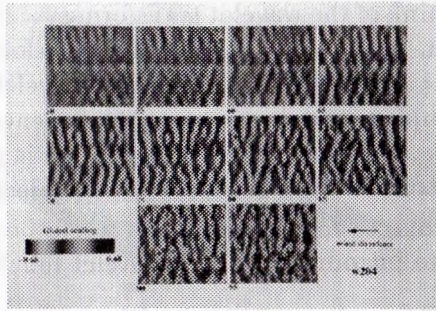
Fig. 2. Time sequence of surface slope values computed from the ISG measurements, numbered in frames. Since the sampling rate, determined by the video framing rate, is 30Hz, the total sequence, occupying 45 frames, covers 1.5 seconds. The doppler-shifted group velocity is such that an entirely new wave field is covered every 15 frames. The color bar is scaled to cover the maximum and minimum slope symmetrically about zero at the last time step in the sequence. (See colour plate 7).

ticles in suspension that scatter the light so that its intensity decreases with downstream distance. In the absence of any surface deformation, light rays pass normal through the surface and the CCD illumination is also homogeneous in y, monotonically decreasing in x. A nonzero surface slope in x (s_x) causes light rays to be refracted and arrive at a different x location on the sensor array. Thus, given the intensity distribution on the array, it is possible to compute the deflection and, hence, the value of s_x at each position in $\{x, y\}$. With careful calibration procedures (Jähne and Schultz, 1992), this calculation can be performed so as to reduce errors due to nonlinear effects to less than $0.05 \mid s_x \mid$.

Fig. 2 shows a time sequence of s_x over a 1.5 second period, during which time the mean and maximum slopes increase by more than a factor of 10. Even at early times, the wave field is never strictly one-dimensional, or uniform in y. It is unclear as to how much this reflects the inhomogeneity of the original forcing. At frame #70, $s_x(x, y)$ reaches its most ordered state, in which the spanwise correlation length is a maximum. After this, the spanwise correlation length decreases, and shortly after the end of this sequence the wave field becomes quite disordered, as noted originally by Kawai (1979), and more recently in Spedding *et al.* (1993).

3   2D Wavelet functions for 2D data

A very readable introduction (Meyer, 1993) and review of wavelet applications (Rushai *et al.*, 1992) have recently become available, and the specific design and application of 2D wavelet functions for analysis of 2D real signals is discussed in Dallard and Spedding (1993). Denoting $f_W(a, \vec{b})$, as the wavelet transform (WT) of the function $f(\vec{x})$, a is the analysing wavelet scale, and resonance at any particular value of a can be related to a wavenumber $\vec{k}$ in the signal. This information is *localised* at a shift from the origin, $\vec{b}$, equivalent to physical

location $\vec{x}$.

It is convenient to think of the wavelet transform as a product in Fourier space of the wavelet function $\hat{g}(a\vec{k})$ with the Fourier-transformed signal, $\hat{f}(\vec{k})$, and Dallard and Spedding (1993) introduced the *Arc* wavelet as a smooth function for general use in a complex, non-directional specific, energy-conserving WT for *2D* data analysis. Here, the alongwind surface slope is $s_x = \partial s/\partial x$, and since $s_x(x, y)$ also contains contributions from $s_y(x, y)$ projected on x, the response ought to be weighted by $\cos\theta$, where θ is the angle between $\vec{k}$ and the mean wind, U_∞. We therefore introduce the *Cos* wavelet function:

$$\vec{k} \in \pi^1 \;:\; \hat{g}(a\vec{k}) \;=\; \hat{g}(a\vec{k}) = \cos\theta \exp\left(-\frac{a^2\sigma^2(|\vec{k}| - |\vec{k}_0|/a)^2}{2}\right)$$

$$\vec{k} \in \pi^2 \;:\; \hat{g}(a\vec{k}) \;=\; 0, \tag{1}$$

where $\theta = (\vec{k}_x, \vec{k})$. It describes a cosine-weighted arc in wavenumber space with Gaussian cross-section, centred at, and shifted from the origin by $|\vec{k}_0|/a$, with width $1/(\sigma a)$. Isometric surfaces of the *Cos* function in wavenumber and physical space are shown in Fig. 3. Owing to the smooth decay in $\hat{g}_{Cos}$, g_{Cos} has improved localisation in physical space over the original g_{Arc}.

The *Cos* WT can be computed at each time step from $s_x(x, y)$, and the result can be expressed as the amplitude $|f_W(a, \vec{b})|$, and the phase, $\angle f_W(a, \vec{b})$ of the complex WT.

4   How to calculate $\vec{\omega}(\vec{k})$ from $f_W(a, \vec{b}, t)$

Since one has local phase information from the complex WT, then the vector field $\vec{u}$ that performs the mapping of,

$$\angle f_W(a, \vec{b})_{t_1} \xrightarrow{\vec{u}} \angle f_W(a, \vec{b})_{t_2}, \tag{2}$$

where $\angle f_W(a, \vec{b})$ is known at two closely-spaced time steps, t_1, t_2, can be used to estimate a local frequency. Since $\vec{u}$ is measured at fixed wavelet scale, a, it is associated with wavenumber $|\vec{k}|$, and

$$\vec{\omega} = |\vec{k}|\,\vec{u}. \tag{3}$$

Various methods can be devised for computing $\vec{u}$. Although details will not be given here, a hybrid scheme using a novel combination of optical flow and cross-correlation methods was found to work reliably. Jähne (1991) can be consulted for overviews of each of these classes of methods separately. The *2D* spatial cross-correlation seeks to find the local displacement, $\vec{r}$, at discrete interrogation windows, such that

$$C(\vec{r}) = \sum_{\vec{x} \in R} f(\vec{x}, t_1) f(\vec{x} + \vec{r}, t_2) \tag{4}$$
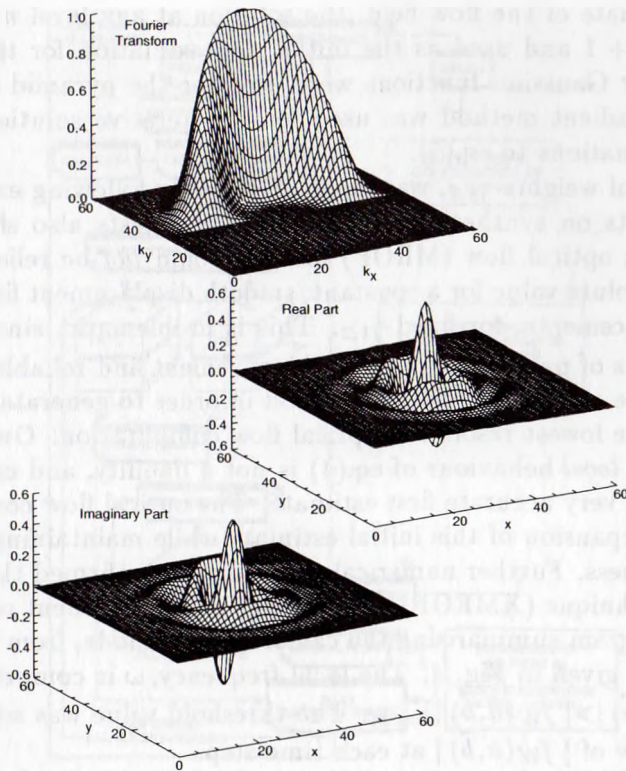
Fig. 3. The *Cos* wavelet function in Fourier space (a), and its real and imaginary parts (b) & (c) in physical space.

is maximised, and then

$$\vec{u} = \vec{r}/(t_2 - t_1).$$

However, simple solutions to this problem blow up in the presence of the *local* phase discontinuities of $\pm\pi$ found in $\angle f_W(a, \vec{b})$, and it is desirable to find some globally smooth solution, such as commonly computed using optical flow techniques.

$\vec{u}$ was computed using a modification of the technique of Zhou *et al.* (1995) who kindly made available their original codes. We proceed by minimising the cost function,

$$e(\vec{u}) = \int_\Omega \{e_I(\vec{u}) + \gamma_1 e_s(\vec{u}) + \gamma_2 (\nabla.\vec{u})^2\}d\Omega. \tag{5}$$

$e_I(\vec{u})$ and $e_s(\vec{u})$ are terms related to the L_2 error, and the smoothness (both global terms), respectively, and γ_1 and γ_2 are weightings on the smoothness, and a divergence-free constraint that was introduced by Zhou *et al.* (1995) for fluid flow applications.

When the displacement field due to $\vec{u}$ is large compared to the grid resolution, a multiresolution relaxation method is used to avoid convergence on local minima in eq.(5). Beginning from the original data, successive binary expansions

are performed until the local displacements do not exceed one mesh size. Given an initial estimate of the flow field, the solution at any level n is interpolated out to level $n + 1$ and used as the initial approximation for the $n + 1^{th}$ iteration. Circular Gaussian functions were used for the pyramid expansion, and a conjugate-gradient method was used for the iterative solution of successive linear approximations to eq.(5).

The choice of weights $\gamma_{1,2}$, was made empirically following extensive numerical experiments on synthetic wave fields. These tests also showed that the multiresolution optical flow (MROF) method could *not* be relied upon to give the correct absolute value for a constant, smooth displacement field, over a large range of displacements, for fixed $\gamma_{1,2}$. This is problematic, since the variation of $\vec{u}$ with $| \vec{k} |$ is of particular interest. A convenient and reliable solution turns out to be to use a cross-correlation method in order to generate the initial first estimate for the lowest resolution optical flow computation. Owing to the grid expansion, the *local* behaviour of eq.(4) is not a liability, and one immediately benefits from a very accurate first estimate. The optical flow computation then preserves an expansion of this initial estimate while maintaining a γ_1-weighted global smoothness. Further numerical experiments confirmed the robustness of this hybrid technique (XMROF) over a range of displacement magnitudes.

A block diagram summarising the calculation methods, from initial digitised data to $\vec{\omega}(\vec{k})$ is given in Fig. 4. The local frequency, ω is computed from eq.(3) for all $| f_W(a,\vec{b}) | > | f_W(a,\vec{b}) |_{thresh}$. The threshold value was set to 80% of the maximum value of $| f_W(a,\vec{b}) |$ at each time step.

Extensive numerical simulations were performed on synthetic data fields, and on $\angle f_W(a,\vec{b})$ derived from real data, but given a known form of $\vec{\omega}(\vec{k})$. These results will be reported in detail elsewhere. In general, the mean difference between spatially-averaged estimates of $\vec{\omega}(\vec{k})$, and the true value, was always less than 5% in ω and less than 10% in $| \vec{k} |$. In conditions closely matching the experimental signal to noise ratios and resolution in $\vec{x}$ and t, the mean errors were about half that.

5   Time dependent, local, dispersion relation for wind-generated surface waves

Although measurements are available for $\vec{\omega}(| \vec{k} |, x, y)$, they will be averaged over $\{x, y\}$ and plotted only for $| \vec{\omega} |$ for brevity and ease of comparison. This dispersion relation is plotted for 3 time steps in Fig. 5(a-c). Fifteen frames separate each plot, which therefore represents data from a completely new wavefield that has convected into the measuring location. The measured data points can be compared with the dispersion relation that can be derived from the linearised momentum and continuity equations at the interface, as given by Caponi *et al.* (1992),

$$\omega = \sqrt{(gk(1 - \alpha) + \sigma k^3)}, \tag{6}$$

where α is the ratio of air to water density ($= 1.21 \times 10^{-3}$), g is the acceleration due to gravity, and σ is the surface tension (74 cm^{3}s^{-2}). The measured phase
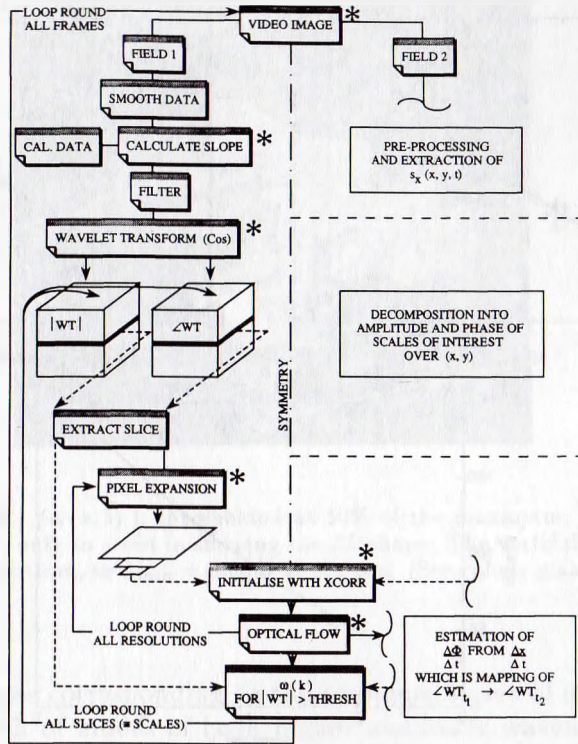
Fig. 4. Block diagram summary of the method for calculating $\bar{\omega}(|\vec{k}|)$ from $s_x(x, y)$. Currently, the minimum Δt is determined by the video framing rate. The two video fields are treated identically on either side of the line of symmetry in the block diagram, until the XMROF method combines both sides to calculate $\angle WT_{t_1} \leftarrow \angle WT_{t_2}$. All boxes marked with an asterisk include state-of-the-art advances in analytical techniques from the last two years.

speeds are doppler-shifted by the water drift velocity at the surface, U_0. Since we lack accurate simultaneous measurements of U_0, a constant offset is added to place the solid curve on the data point occurring at the predicted most amplified wave, at $k_0 = 3.63$ rad/cm (An independent measurement of the wavenumber of the most amplified wave from the spatially-averaged centroid of the $|WT|^2$ gives $k_0 = 3.67 \pm 0.05$ rad/cm). This offset gives a drift current of 14 cm/s, which is consistent with previous results reported for this facility (Huang, 1992), but at $0.027U_\infty$ is significantly below the 0.05 or $0.04U_\infty$ sometimes assumed in the literature.

The measured $\omega(|\vec{k}|)$ in Fig. 5a agrees with the theoretical prediction to within experimental uncertainty over the whole range of $|\vec{k}|$ where there is significant energy. At the next time step (Fig. 5b), the range of energetic $|\vec{k}|$ has contracted around k_0, consistent with qualitative observations made earlier for Fig. 2 at t=65/70. The agreement with the linear theory over this range remains good. At t=80, the range of energetic modes is significantly expanded,
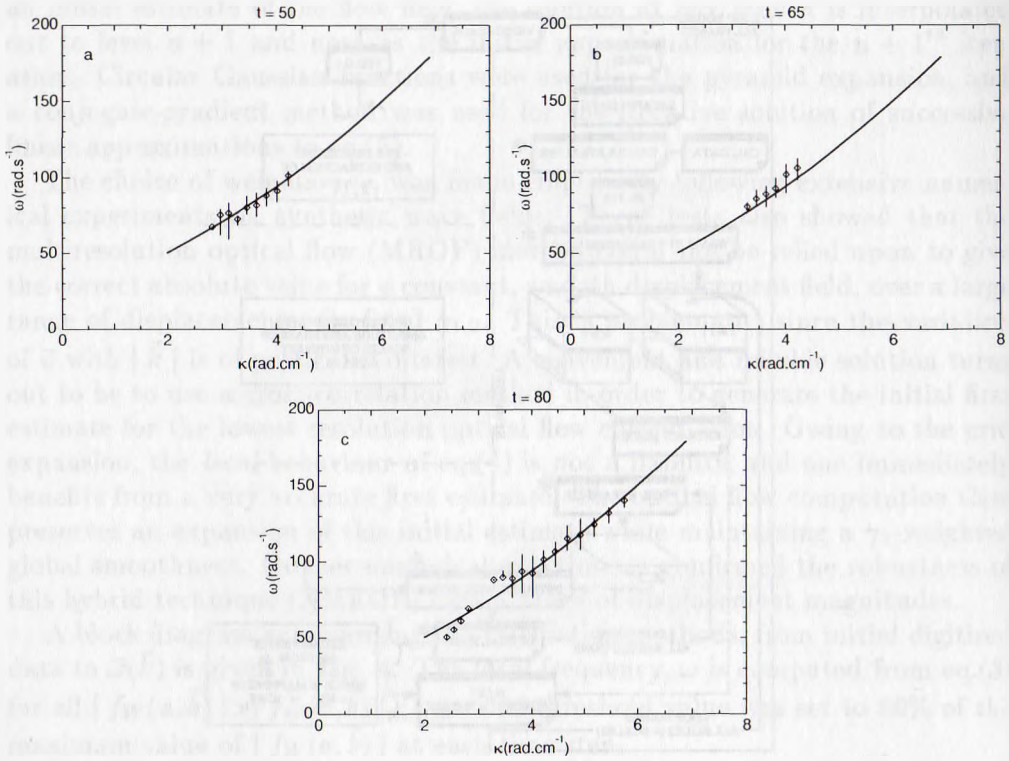
Fig. 5.   Evolution of the dispersion relation for the wind-generated surface wave field of Fig.
2. (a) t=50, (b) t=65, (c) t=80. Diamonds are the mean measured values at each $|\vec{k}|$. The
solid line is the linear stability result. It is drawn over the whole range of k for which the WT
was computed.

with energy having appeared in both lower and higher wavenumbers. It is
greatly reduced around k_0. Above k_0, eq.(6) predicts the data well, but there is
increased scatter and difference between the two at, and below k_0.

6   Discussion and Conclusions

The simple relationship of eq.(6) from 1-D linear theory appears to hold well
until the latter stages of the sequence discussed here, despite the fact that the
wavefield is never strictly 1-D (i.e. spanwise uniform). Nevertheless the initial,
most unstable wavelength is well predicted. Caponi et al. (1992) include a dis-
cussion of the time-varying interpretation of their analytical results, which were
obtained from piecewise linear approximations to the wind and water velocity
profiles, although the solution itself did not involve time-dependent growth of
these profiles. Quite specific predictions are made concerning the growth rates
and most unstable modes at different wind speeds and we look forward to mak-
ing detailed comparisons over the same parameter range. The results of Kawai
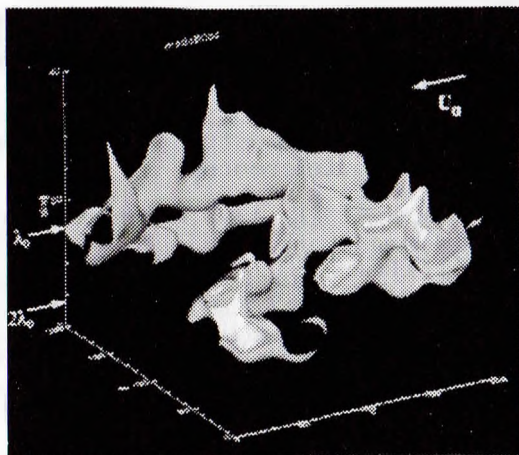(1979) thus far appear to be confirmed in the current study, and will also be

Fig. 6.   Isosurface of $| f_W(a, b) |$, thresholded at 50% of the maximum, for t=80. Surface intensity variations are only to assist in showing the *3D* shape. The vertical scale, a runs from $\lambda_{max} = 4.6$cm at the bottom, to $\lambda_{min} = 0.6$cm at the top. (See colour plate 8).

compared further.

At the later stages corresponding to the presumed onset of nonlinear effects, we note here growth of modes of both higher *and* lower wavenumber than k_0. This is illustrated in Fig. 6, where it appears that growth of these modes occurs in closely associated spatial locations. Although an earlier, preliminary wavelet analysis (Spedding *et al.*, 1993) indicated that significant energy developed in subharmonic wavelengths, the improved resolution and quantitative accuracy of the current data allow the distinction to be made that the majority of the sideband growth actually occurs in bands centred at $\frac{2}{3}k_0$ and $\frac{4}{3}k_0$. The sum of these is $2k_0$, consistent with the resonance frequency condition for a Benjamin-Feir type instability. However, Bliven *et al.* (1986) suggested that this mechanism is suppressed by active wind forcing, and it is unlikely to be significant at this scale range. There is an alternative, simple physical interpretation, that asymmetric steepening and growth of single wave crests is manifested as different modes, which would then necessarily be correlated in physical space.

In this case, the natural tendency to think in terms of Fourier modes, or their spatially localised, wavelet-based cousins, may be unnecessarily restrictive. It could prove interesting instead to allow the wavelet function basis itself to auto-adapt with time, similar in spirit to the work of Coifman *et al.* (1992) and Wickerhauser (1992).

7   Acknowledgements

References

Bliven, L. F., Huang, N. E., and Long, S. R.: 1986, 'Experimental Study of the Influence of Wind on Benjamin-Feir Sideband Instability', *J. Fluid Mech.* **162**, 237-260.

Caponi, E. A., Caponi, M. Z., Saffman, P. G., and Yuen, H. C.: 1992, 'A Simple Model for the Effect of Water Shear on the Generation of Waves by Wind', *Proc. R. Soc. Lond. A* **438**, 95-101.

Coifman, R. R., Meyer, Y., and Wickerhauser, V.: 1992, 'Wavelet Analysis and Signal Processing', in M. B. Ruskai, G. Beylkin, R. Coifman, I. Daubechies, S. Mallat, Y. Meyer, and L. Raphael (eds.), *Wavelets and their Applications*, Jones and Bartlett, Boston, pp. 153-178.

Dallard, T., and Speeding, G. R.: 1993, '2-D Wavelet Transforms: Generalisation of the Hardy Space and Application to Experimental Studies', *Eur. J. Mech. B/Fluids* **12**, 107-134.

Huang, N. E.: 1992, ' Laboratory Investigations of Ocean Surface Roughness Generation', in A. Brandt, S. E. Ramberg, and M. F. Shlesinger (eds.), *Nonlinear Dynamics of Ocean Waves*, World Scientific Press, Singapore, pp. 128-149.

Jähne, B., and Riemer, K.: 1990, ' Two-Dimensional Wave Number Spectra of Small-Scale Water Surface Waves', *J. Geophys. Res.* **95**, 11,531-11,546.

Jähne, B.: 1991, *Digital Image Processing. Concepts, Algorithms and Scientific Applications*, Springer-Verlag, Berlin, pp. 275-317.

Jähne, B., and Schultz, H.: 1992, 'Calibration and Accuracy of Optical Slope Measurements for Short Wind Waves', *Optics of the Air-Sea Interface: Theory and Measurements, SPIE.*

Kawai, S.: 1979, 'Generation of Initial Wavelets by Instability of a Coupled Shear Flow and their Evolution to Wind Waves', *J. Fluid Mech.* **93**, 661-703.

Long, S. R.: 1992, *NASA Wallops Flight Facility: Air-Sea Interaction Research Facility, NASA GSFC/WFF, Wallops Island, VA, Report no. 1277.*

Miles, J. W.: 1957, 'On the Generation of Surface Waves by Shear Flows', *J. Fluid Mech.* **3**, 185-204.

Miles, J. W.: 1959, 'On the Generation of Surface Waves by Shear Flows, Part 2', *J. Fluid Mech.* **6**, 568-582.

Meyer, Y.: 1993, *Wavelets: Algorithms and Applications*, SIAM, Philadelphia.

Phillips, O. M.: 1957, 'On the Generation of Waves by Turbulent Wind', *J. Fluid Mech.* **2**, 417-445.

Phillips, O. M.: 1977, *The Dynamics of the Upper Ocean*, Cambridge University Press, Cambridge.

Press, W. H., Teukolsky, S. A., Vetterling, W. T., and Flanner, B. P.: 1992, *Numerical Recipes in FORTRAN : The Art of Scientific Computing, Second Edition*, Cambridge University Press, Cambridge, pp. 565-569.

Ruskai, M. B., Beylkin, G., Coifman, R., Daubechies, I., Mallat, S., Meyer, Y., and Raphael, L. (eds.): 1992, *Wavelets and their Applications*, Jones and Bartlett, Boston.

Spedding, G. R., Browand, F. K., Huang, N. E., and Long, S. R.: 1993, 'A 2-D Complex Wavelet Analysis of an Unsteady Wind-Generated Surface Wave Field', *Dyn. Atmos. Ocean* **20**, 55-77.

Wickerhauser, M. V.: 1992, 'Acoustic Signal Compression with Wavelet Packets', in C. K. Chui (ed.), *Wavelets - A Tutorial in Theory and Applications*, Academic Press, San Diego, pp. 679-700.

Zhou, Z. Y., Synolakis, C. E., Leahy, R. M., and Song, S. M.: 1995, 'Calculation of 3-D Internal Displacement Fields from 3-D X-Ray Computer Tomographic Images', *Proc. Roy. Soc. Lond.* **A**, **449**, 537-554.